

Mesoscale characteristics

G. A. Jacobs, C. N. Barron, and R. C. Rhodes

Naval Research Laboratory, Stennis Space Center, Mississippi, USA

Abstract. The spatial length, time, and propagation characteristics of the ocean mesoscale variability are examined throughout the globe. Sea surface height (SSH) variations from a combination of the Geosat Exact Repeat Mission, ERS-1, ERS-2, and TOPEX/Poseidon altimeter satellites are used to compute the observed covariance of the mesoscale. The mesoscale is defined as the residual SSH after removing a filtered large-scale SSH having length scales greater than 750 km zonally and 250 km meridionally. From the observed binned covariance function, an objective analysis computes characteristics of the climatological mesoscale variability. Westward propagation is dominant throughout the globe. The Antarctic Circumpolar Current appears to affect the zonal propagation, as the propagation direction is eastward throughout this current. Length scales and propagation speeds generally decrease away from the equator and are slightly larger in the west basin areas than in the east basin areas. Zonal propagation speeds are roughly in agreement with speeds based on linear quasi-geostrophic dynamics. The eddy field diverges from the equator and converges at 15° in the Northern and Southern Hemispheres. Requirements for synoptic mesoscale observation are examined.

1. Introduction

Characterization of the mesoscale variability is important to generate optimal ocean state estimates for monitoring and prediction systems, to independently evaluate models, and to understand how factors that influence the mesoscale characteristics vary throughout the globe. The mesoscale characteristics have been described through many methods. Beginning with in situ current meter moorings and hydrographic observations, the Mid-Ocean Dynamics Experiment (MODE), POLYGON MODE (POLYMODE), and Tourbillon experiments provide insight into the North Atlantic mesoscale dynamics. *Richman et al.* [1977] use temperature and current meter data from the MODE experiment to determine length scales and elucidate eddy dynamics. *McWilliams et al.* [1986] and *Hua et al.* [1986] use current meter data from the POLYMODE Local Dynamics Experiment (LDE) to statistically estimate stream functions at different depths in order to observe the spatial and vertical eddy structure. *Le Groupe Tourbillon* [1983] and *Mercier and de Verdiere* [1985] use the Tourbillon experiment current meter observations of the Porcupine basin to examine the eddy variability. These experiments have provided some of the first estimates of the mesoscale characteristics as well as valuable insight into the dynamical processes. In situ measurements can provide an intensive examination of the horizontal and vertical velocity, temperature, and salinity distributions associated with the mesoscale structure. One disadvantage to in situ measurements is that they are difficult to obtain and therefore are often relatively limited in space and time.

With a growing abundance of satellite data, characterization of the eddy field has greatly expanded. *Halliwel and Mooers* [1979] use sea surface temperature (SST) frontal analysis to examine Gulf Stream eddies through time-space lagged covariance. *Auer* [1987] constructs a statistical census of Loop Current eddies, Gulf Stream warm and cold core ring events, and associated characteristics. The advanced very high resolution radiometer (AVHRR) derived SST allows an excellent two-dimensional view of the ocean surface. One drawback is the observational masking created by clouds. In addition, effects such as the uniform summer Gulf of Mexico temperatures mask eddy events [*Auer*, 1987]. This drawback occurs because the SST is not a direct dynamical quantity. Rather, the ocean circulations as well as a number of additional variables such as solar radiation, latent and sensible heat fluxes, and vertical mixing from wind influence the SST.

The altimeter-observed sea surface height (SSH) is a direct measure of the ocean height contribution to surface pressure and is thus a direct measure of a dynamical variable. The Seasat suite of sensors included an altimeter of sufficient accuracy to measure ocean mesoscale variations. Some of the first global variability distributions were computed from Seasat data [*Cheney et al.*, 1983; *Fu*, 1983]. Owing to its short life span, the satellite was not able to produce long time period statistics. Altimeter satellites are generally constrained to an exact repeat orbit, and there have been three main repeat orbits used to date (Figure 1). The Geosat Exact Repeat Mission (ERM) altimeter provided data of sufficient accuracy and temporal length for many examinations of both the mesoscale field and seasonal changes in the field [*Zlotnicki et al.*, 1989].

The TOPEX/Poseidon (T/P) altimeter has provided the most accurate sea level variation data to date [*Fu et al.*, 1994]. However, the T/P ground track spacing is relatively large (314 km between parallel tracks at the equator) and does not

This paper is not subject to U.S. copyright. Published in 2001 by the American Geophysical Union.

Paper number 2000JC000669.

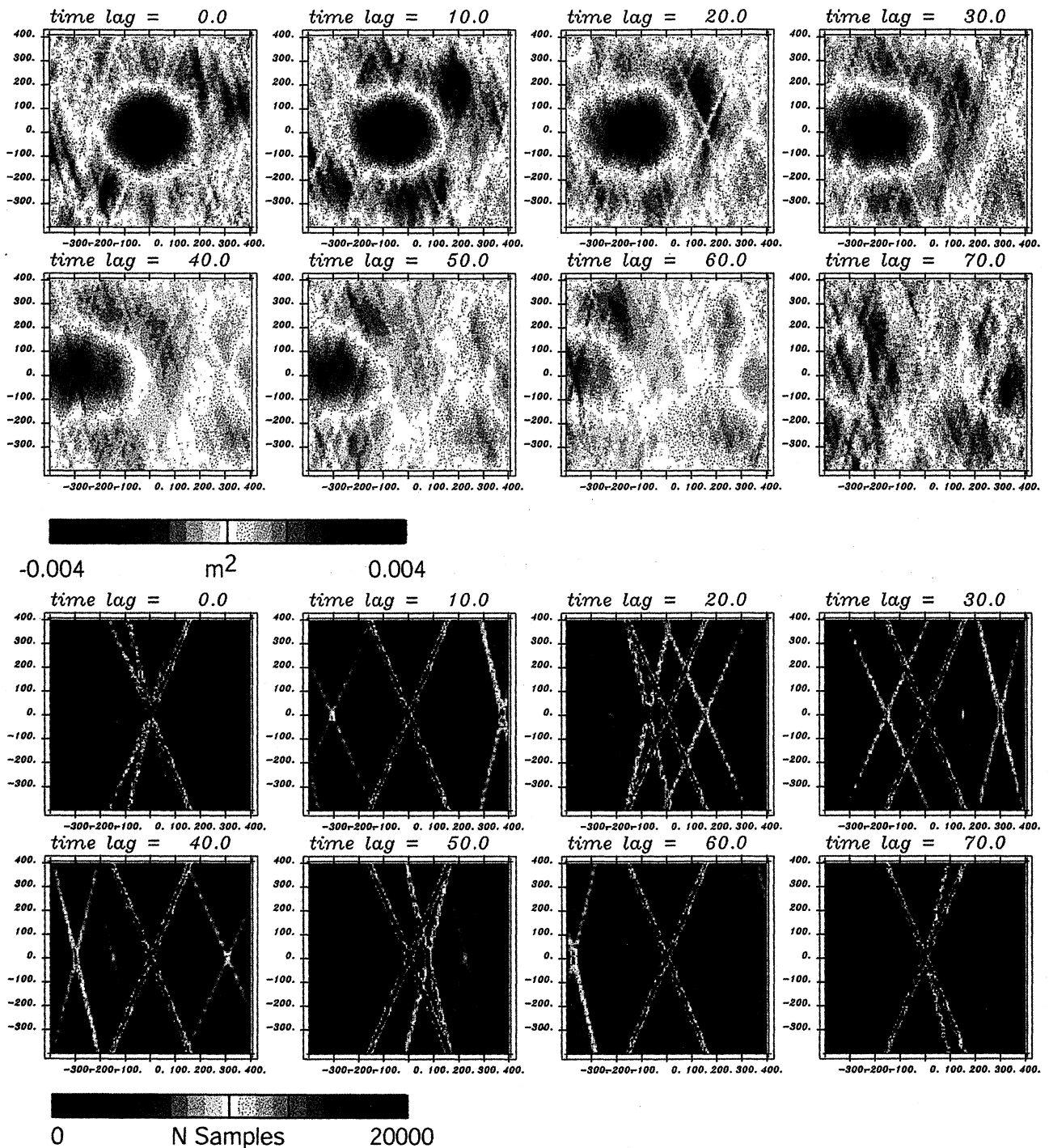


Plate 1. (top) Binned covariance and (bottom) number of samples in the binned covariance are determined from T/P, ERS-1, ERS-2, and Geosat ERM altimeter data. The covariance functions are generated on a regular 2° grid throughout the globe. The spatial bin size is 10 km in both the meridional and zonal directions. The temporal bin size is 2.5 days (not every time lag is shown). The binned covariance function at $20^\circ N$, $160^\circ E$ indicates length scales of about 150 km. In 60-days' time, the center of the peak covariance progresses westward about 350 km (a 6.75-cm/s propagation speed). The number of samples within each bin of the covariance function is strongly biased toward the altimeter ground tracks. However, the number of samples within each bin is generally above 2000.

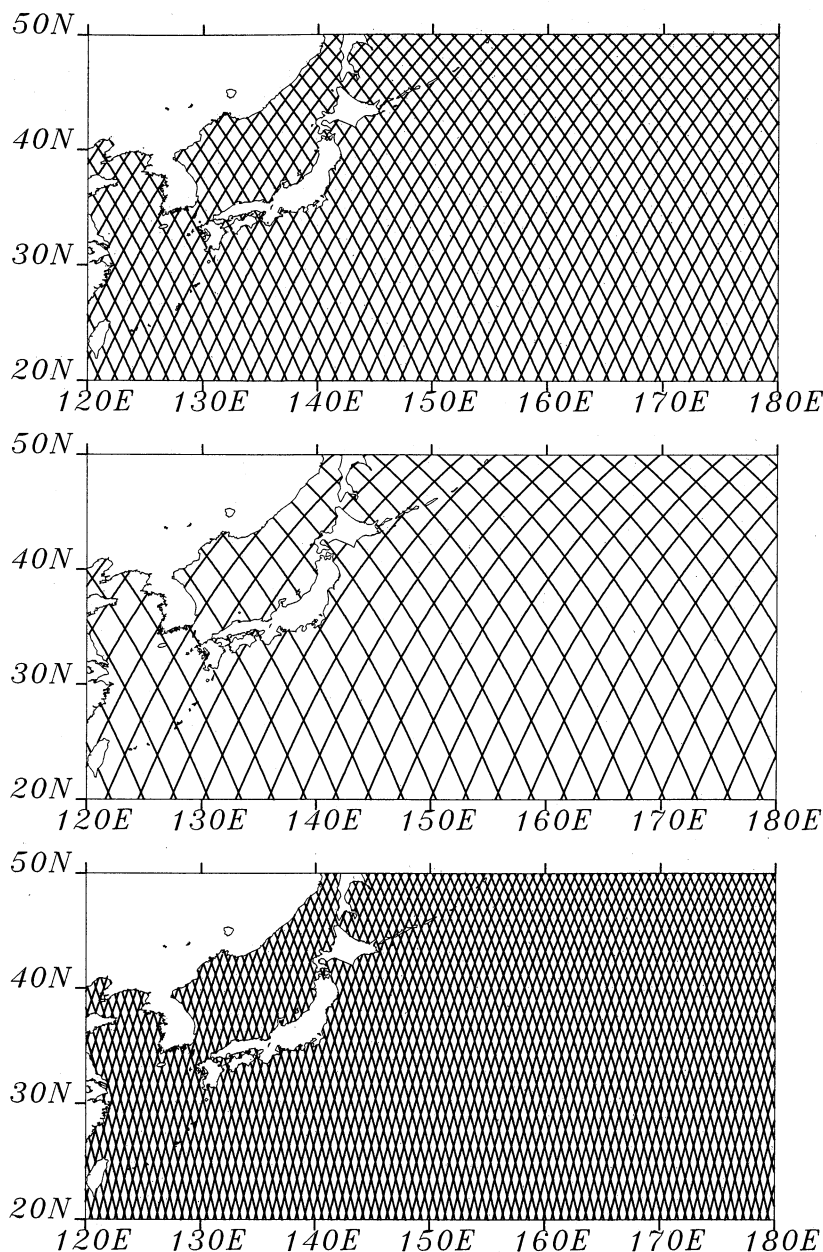


Figure 1. Ground track patterns of the (top) Geosat Exact Repeat Mission, (middle) TOPEX/Poseidon, and (bottom) European Remote Sensing satellite provide different compromises for spatial and temporal sampling capabilities. Over 1 day, each satellite provides about the same amount of information.

resolve the expected eddy scales at middle to high latitudes. The European Remote Sensing Satellites (ERS-1 and ERS-2) have provided data of comparable quality with much higher spatial resolution though much longer repeat period between samples.

The leap from in situ data to remote satellite observations has suffered from the lack of vertical dynamic characterization of the eddy field. The baroclinic instability largely responsible for eddy generation within western boundary currents and associated extensions may not be examined through surface observations alone. There have been many studies designed to evaluate altimeter capabilities relative to in situ measurements and understand the dynamics relating the eddy field to the sea surface height. *Hallock et al.*

[1989] use inverted echo sounders (IES) in the Gulf Stream beneath the Geosat ERM ground tracks for direct comparison. *Teague et al.* [1995] perform similar studies in the Kuroshio Extension beneath T/P ground tracks. *Ichikawa and Imawaki* [1994] examine a shed Kuroshio ring using the Geosat ERM data along with conductivity-temperature-depth (CTD) and SST data for verification. *Gilson et al.* [1998] compare the T/P data with a set of CTD data along a transect crossing the North Pacific Ocean, and *McCarthy et al.* [2000] perform a similar examination across the South Pacific Ocean.

The methods used to extract the mesoscale characteristics from altimeter data have covered a wide range. One of the most direct methods for deriving length scales is from the along-track wave number spectra and associated along-track

correlation [Fu and Zlotnicki, 1989; Le Traon et al., 1990; Stammer and Boning, 1992; Stammer, 1997]. This method provides excellent estimates of length scales but does not allow estimates of propagation speed or direction. Constructing gridded data sets and examining the variations at particular latitude bands [Tai and White, 1990; Aoki and Imawaki, 1996; Gilson et al., 1998] allows estimation of zonal speed as well as zonal length scales. Halliwell et al. [1991] use Geosat and SST in time-space lagged covariance and variations at particular latitude bands to show 800-km waves in the southern Sargasso Sea. However, the results depend on the gridding and filtering methodologies and do not provide meridional length scale or propagation speed. By using the three-dimensional correlation structure, estimates may be made of the timescale, zonal and meridional length scales, and propagation speeds [Kuragano and Kamachi, 2000].

The mesoscale field characterization has grown in incremental steps over the past 25 years as new technology has expanded observations. This analysis examines the mesoscale field through a combination of altimeter data from T/P, ERS-1, ERS-2, and the Geosat ERM to generate the observed binned covariance function. From the binned covariance function, an objective analysis computes parameters for eddy length scales, propagation speeds, and timescales. The spatial and temporal data density is increased by using not only the covariance of each satellite data set with itself but also the cross covariance between ERS-1, ERS-2, and T/P. Binned covariance functions are computed every 2° in latitude and longitude. The mesoscale parameters are derived from each binned covariance function on this 2° grid so that spatial variations in the mesoscale character may be observed.

Before beginning the detailed examination, the mesoscale must be defined. For purposes here, the mesoscale is the residual after removing large-scale variations. The large-scale variability can dominate the ocean sea level anomaly and is due to processes such as the global steric anomaly, basin and gyre scale variations, and large-scale waves. The large-scale variations are computed from the altimeter observations by a simple spatial smoothing using *e*-folding length scales of 750 km zonally and 250 km meridionally. This anisotropic smoothing does not intend to imply that the mesoscale field is anisotropic, but rather the large-scale field is expected to have variations that are more coherent zonally than meridionally. Removal of this large-scale signal inevitably impacts the smaller scales, and the large-scale filter effects on the mesoscale must be examined. The spatially smoothed signal removed is intended to be larger than the expected mesoscale. However, there are regions (particularly in the equatorial areas) where this is not true. Thus a portion of the mesoscale is removed with the large-scale variability.

After a description of the altimeter data sets and removal of the large-scale signal (section 2), a binned covariance function is constructed (section 3). A Gaussian function form is assumed for the covariance function (section 4), and the resulting functional parameter distributions are compared with previous results and linear Rossby wave propagation speeds based on Rossby radii derived by Emery et al. [1984] (section 5). The mesoscale characteristics can be used to derive the requirements for mesoscale field sampling by altimeter satellites (section 6).

2. Altimeter Data Sets

The data used in this analysis are from the Geosat ERM, ERS-1, ERS-2, and T/P altimeter data sets. The T/P merged Geophysical Data Records (GDR) are provided by the Physical Oceanography Distributed Active Archive Center at the Jet Propulsion Laboratory. Data from both the TOPEX and Poseidon instruments are treated similarly. The near real-time ERS-1 and ERS-2 data are provided by the National Oceanic and Atmospheric Administration (NOAA). Because of the many changes in orbital configuration, ERS-1 data are used only from the launch time of the ERS-2 mission onward. NOAA also provides the Geosat ERM GDRs. Each data set is processed in a similar manner independently of one another. The dry troposphere, wet troposphere, ionosphere, and electromagnetic bias corrections are obtained from the GDRs and are applied to the SSH measurements. The FES-95.2 tide model [Le Provost et al., 1994] is used to remove ocean tides from each of the satellite data sets. Altimeter data taken over water depths of less than 2000 m are removed before the analysis. Wind-driven sea level setup variations strongly influence sea surface height on the continental shelf. The signals from these variations can be larger than the mesoscale field in the open ocean and would cause significant contamination if not removed.

For each satellite, ground tracks are defined as one full satellite revolution. Repeat passes over the same ground track are grouped together. Interpolation of each collinear repeat pass along the track is made to reference points separated by 1-s intervals. Because of the relatively large orbit errors in the Geosat ERM data, an empirical orbit error removal is required. The empirical orbit error correction for each repeat pass is a removal of a one cycle per orbital revolution sinusoid relative to the mean sea level along the ground track. The climatologically observed seasonal variations of the global dynamic height anomaly are used to minimize corruption of the expected global scale ocean variability. The Generalized Digital Environmental Map (GDEM) [Teague et al., 1990] provides the seasonal climatology. For each repeat pass, the seasonal climatological dynamic height anomaly relative to 1500 dbar is interpolated and sampled at the satellite latitude, longitude, and time points. The dynamic height is added to the mean sea level along the ground track before orbit corrections are made. Any residual errors or oceanography removed by this empirical orbit error correction are at long wavelengths (40,000 km), which is well separated from the mesoscale length scales, and should not significantly impact estimates of the character of the mesoscale variability.

The T/P and ERS-1/ERS-2 orbit solution errors are much less than those of the Geosat ERM data. However, it is important that the data sets be consistent in terms of their error content. We derive great benefits by including the cross covariance between T/P, ERS-1, and ERS-2 data sets. The inclusion of the Geosat ERM data also provides some benefit. In order to construct one covariance function from these different data sets, it is important that the error structure of all the data sets be as similar as possible. Thus consistency of treatment is important. For example, if the ERS and T/P orbit solution error statistics were different, the autocovariance of each would have different structure along track. For this reason, we apply the same orbit correction to the ERS-1, ERS-2, and T/P data sets.

If the mean sea surface height of each satellite were independently removed, this would not produce sea level variations relative to a consistent mean. If the satellite data sets are to be used simultaneously in estimating the covariance, all three satellite data sets must be referenced to a mean sea level over the same time. The T/P data set covers the entire ERS data time period used here. The T/P sea level variations about its 6-year mean (from January 1993 through December 1998) are interpolated spatially using a simple weighted average where the weighting is provided by a Gaussian function with a 200-km e -folding length scale. The procedure is similar to that of Zlotnicki *et al.* [1989]. The 200-km e -folding length is chosen based on the T/P ground track spacing of about 314 km at the equator. This crude interpolation uses a fixed spatial length scale and no assumption of propagation speed. The errors in the interpolation are larger than those that would result from using the length scales and propagation speeds derived in this analysis. This initial interpolation provides a bootstrapping method. Once an improved estimate of the covariance function is defined, an improved interpolation may be made and an iterative improvement may be constructed. For the results presented here, we use only this simple bootstrap for the analysis.

The interpolated T/P sea level is sampled at the ERS space and time observation points. Since the T/P interpolated data are deviations from the 6-year mean, the ERS height minus the T/P interpolation should be the ERS mean relative to the same 6-year time period:

$$\text{ERS}_{\text{mean}} = (\text{ERS}_{\text{height}} + \text{error}_1) - [\text{Interpolation}(\text{TOPEX}_{\text{height}} - \text{TOPEX}_{\text{mean}}) + \text{error}_2] \quad (1)$$

The error in the ERS_{mean} comes from two sources. First, there are errors in each ERS height measurement (error_1) due to instrument noise, corrections, and orbit solution. Second, there are T/P interpolation errors (error_2) due to inaccuracies of the assumed covariance function in addition to smaller instrument noise contributions. The average of many ERS_{mean} estimates (one estimate for each cycle) reduces the expected ERS_{mean} estimate error. Both ERS-1 and ERS-2 data are used in forming the mean along the ERS ground tracks. Thus about 45 ERS_{mean} estimates are averaged together. The estimated ERS_{mean} is subtracted from the ERS SSH measurements. The resulting ERS SSH anomaly is an estimate of the SSH deviation from the mean over the 6-year T/P time period.

Referencing the Geosat ERM data to the same time period of the T/P data is not possible by the same method used for the ERS data because the Geosat ERM and T/P data do not overlap. Instead, the mean sea level change at points where the Geosat ERM and T/P ground tracks cross is interpolated spatially. This interpolated field is then sampled at the Geosat ERM ground track points so that the Geosat sea level variations are referenced to the 6-year mean sea level of T/P. The details of this procedure and analysis are described by Jacobs and Mitchell [1997].

3. Binned Covariance

As discussed in the introduction, for the purposes of this analysis we define the mesoscale variability as the residual after removing a long-wavelength filtering of the altimeter data. Since this analysis derives mesoscale characteristics

from the binned covariance function, large-scale variability may bias the binned covariance functions and produce unrealistically large length scales. The large-scale signals to be removed include processes such as the global steric anomaly, El Niño, and variations in basin scale gyres. A smoothed SSH is computed from the altimeter data by using a Gaussian weighting with e -folding length scales of 750 km zonally, 250 km meridionally, and a 15-day timescale. All altimeter data are used in the smoothing since all data represent anomalies relative to the same time period and have been processed similarly. The interpolated field is sampled at the time and space locations of each altimeter satellite, and the large-scale interpolated field is removed from the data. The mesoscale field is the residual variability after removing the large-scale interpolation.

The filtering and removal of the large-scale field affect the smaller scales. The potential impact is examined in an idealized case. First, we represent an eddy by an isotropic sea level anomaly with an e -folding scale of 100 km. The eddy is smoothed spatially by the large-scale filter, and the smoothed field is subtracted from the eddy (Figure 2). The same process is computed using idealized eddies with e -folding scales of 200 km and 300 km (Figure 2). The 100-km eddy amplitude is only slightly reduced by the large-scale removal. The 200-km eddy amplitude is reduced to 76% of its original, and the 300-km amplitude is reduced to 57% of its original. In addition, the eddy zonal extent is decreased. From these simple tests, we expect amplitudes of features at length scales much more than 200 km to be significantly damped. In order for an area to be dominated by length scales greater than 200 km after the filtering, there must be very little energy at length scales of less than 200 km. Another effect of the smoothing is that we expect the estimated zonal length scales to be slightly less than the true scales.

A binned covariance function is computed from the altimeter sea surface height variability data on a 2° latitude-longitude grid throughout the globe. The computation at each grid point proceeds identically and separately. First, all altimeter data within a 500-km distance of the given latitude and longitude are selected. Care is taken to avoid data contamination between separate basins. Data from the open Pacific Ocean should not be used in the binned covariance in the Japan/East Sea. Similarly, data in the Caribbean Sea should not influence results in the equatorial Pacific Ocean. To avoid these problems, a set of lines is defined on land masses so that ocean data points falling on opposite sides of a line are not included in the binned covariance.

For the binned covariance, the meridional and zonal lags range from -400 km to 400 km with a resolution of 10 km. The binned covariance temporal lag range extends from 0 to 70 days with a resolution of 2.5 days. Negative time lags are not included, as the binned covariance function is reflectively symmetric about the zero lag point. Each point of the selected data set is related to every other point in the selected data set. To reduce the effects of white noise, the contribution to the covariance function of each point with itself is not included. The effect of white noise is to add a spike at the zero lag point. The zonal, meridional, and temporal lags are calculated, and the contribution of the two points to the binned covariance function is added. The temporal overlap of the T/P and ERS data in conjunction with the simultaneous inclusion in the covariance significantly aids toward filling bins between ground track points.

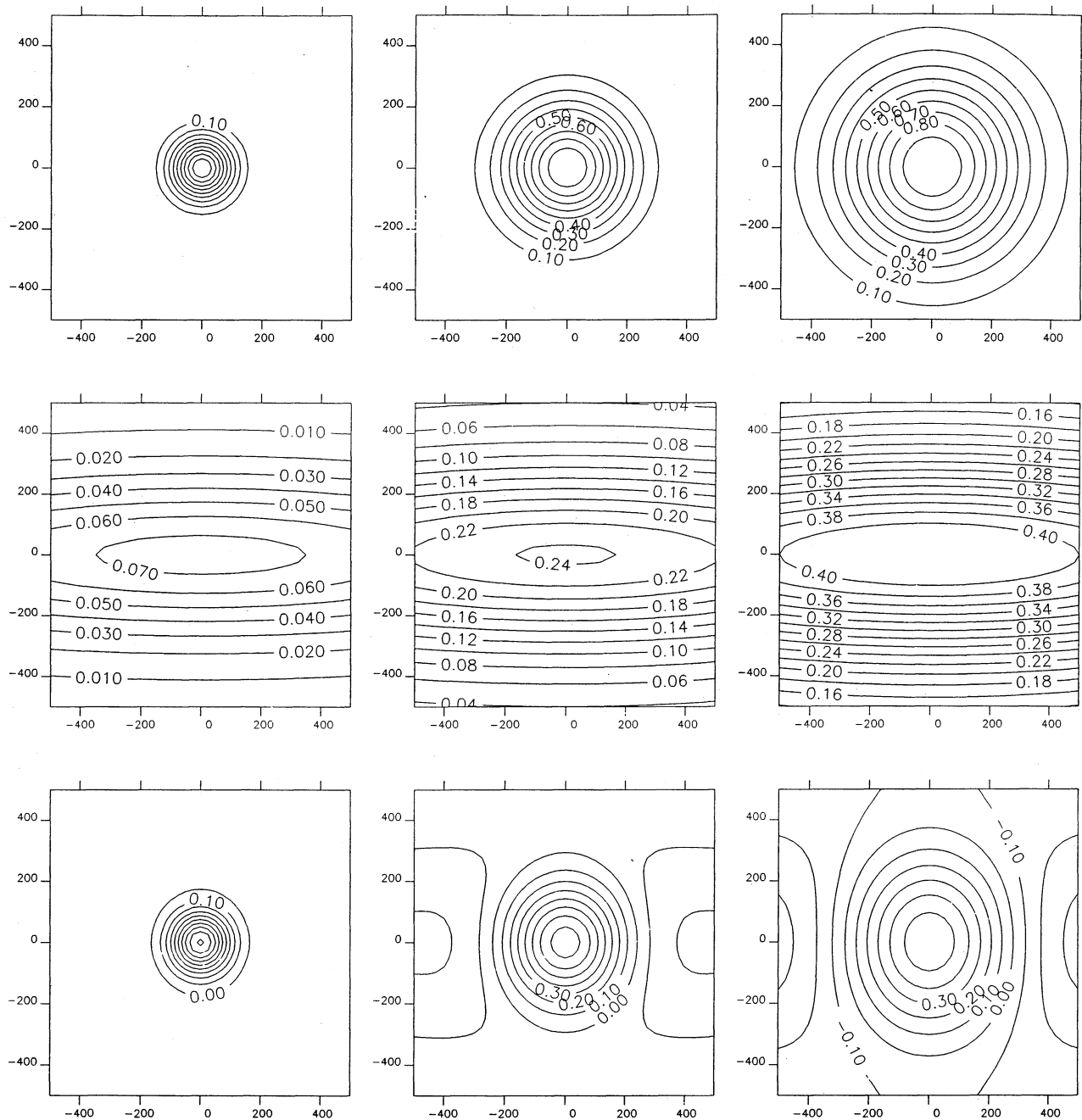


Figure 2. Effects of the large-scale removal are examined on idealized eddies. Eddies are Gaussian functions with (top left) 100-km, (top middle) 200-km, and (top right) 300-km e -folding scales. Large-scale filtering (second row) is subtracted from the original to produce the mesoscale. (bottom left) Distortion to the 100-km eddy is small with only a slight decrease in amplitude and reduction in zonal length scale. (bottom middle) The 200-km eddy amplitude is 76% of the original, and the zonal length scale is further reduced. (bottom right) The 300-km eddy is reduced to 57% of the original amplitude.

During the binning process, the data centroid within each bin is also computed. That is, the average zonal, meridional, and temporal lag within each bin is computed. The reason is that the spatial and temporal sampling are regular and based on the altimeter ground tracks and repeat cycle. Thus we do not expect the data distribution within a particular covariance function bin to be completely random. The covariance value within each bin does not represent the value exactly within the bin center. This information is used when fitting the

functional form to the binned covariance function in section 4.

One example of the binned covariance function is presented in Plate 1. This point is at 20°N, 160°E, a point in the center of the North Pacific subtropical gyre. Not all time lags are presented in this figure. At time lag zero, the covariance indicates spatial scales of about 100 km. Over a 30-day time period, the high-covariance region moves westward about 150 km, the peak amplitude decreases, and the general shape remains similar to the zero time lag. The

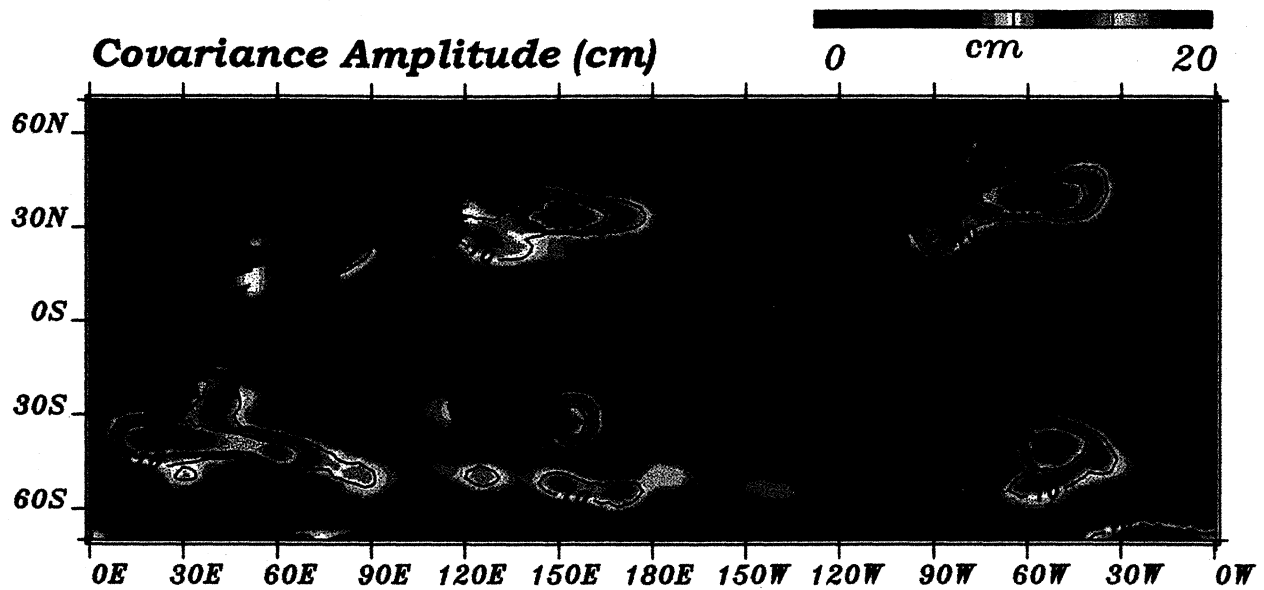


Plate 2. Mesoscale field covariance amplitude is highest in the western boundary current regions. Moderate variability covers the Antarctic Circumpolar Current and eastern portions of the subtropical gyres. Large-scale variability has been removed prior to this calculation; so the variability is lower than the total RMS variability associated with the altimeter data.

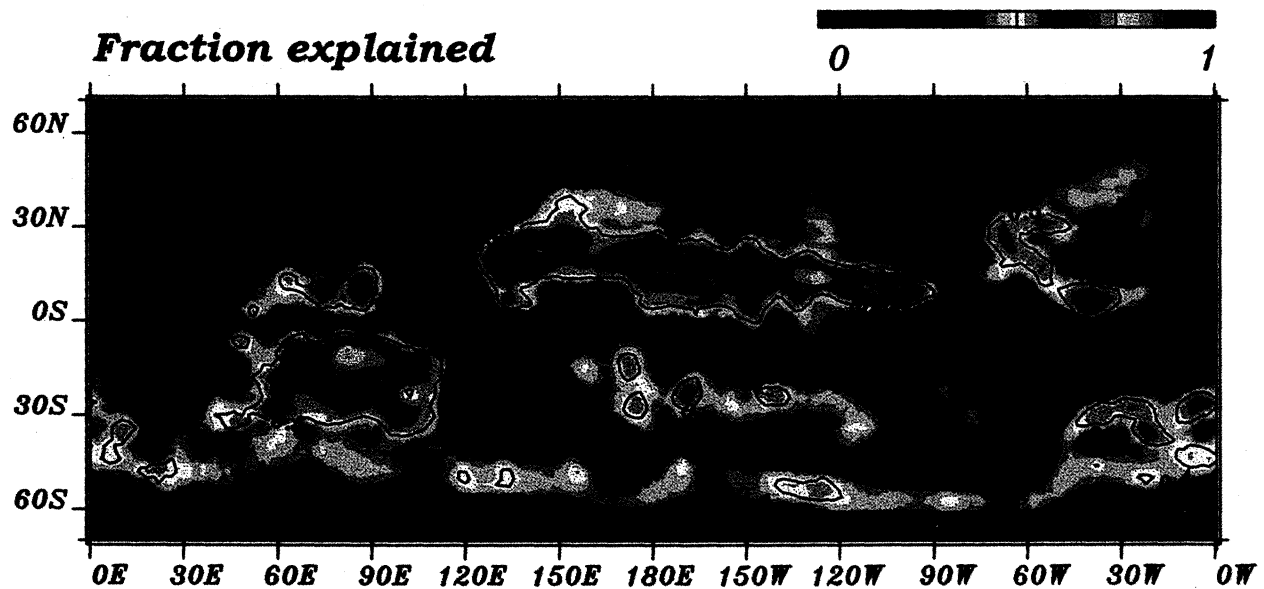


Plate 3. Fraction of the observed binned covariance function explained by the Gaussian fit is largest in the basin centers and decreases near the coasts. The Gaussian function is not capable of representing negative covariance, and the binned covariance shape may differ markedly from the Gaussian shape.

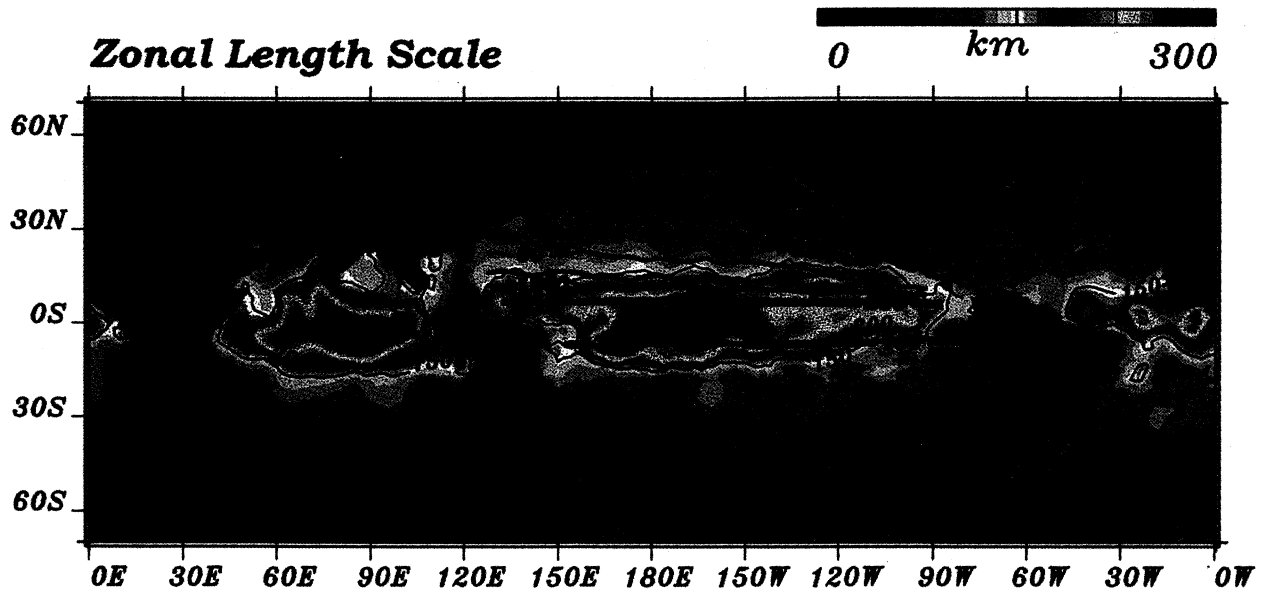


Plate 4. Zonal length scales increase toward the equator. Black contour lines are length scales derived here, and red contour lines in the North Pacific are the Rossby radius of deformation based on results from *Emery et al.* [1984]. Zonal length scales at middle to high latitudes are generally larger than those predicted from the Rossby radius of deformation.

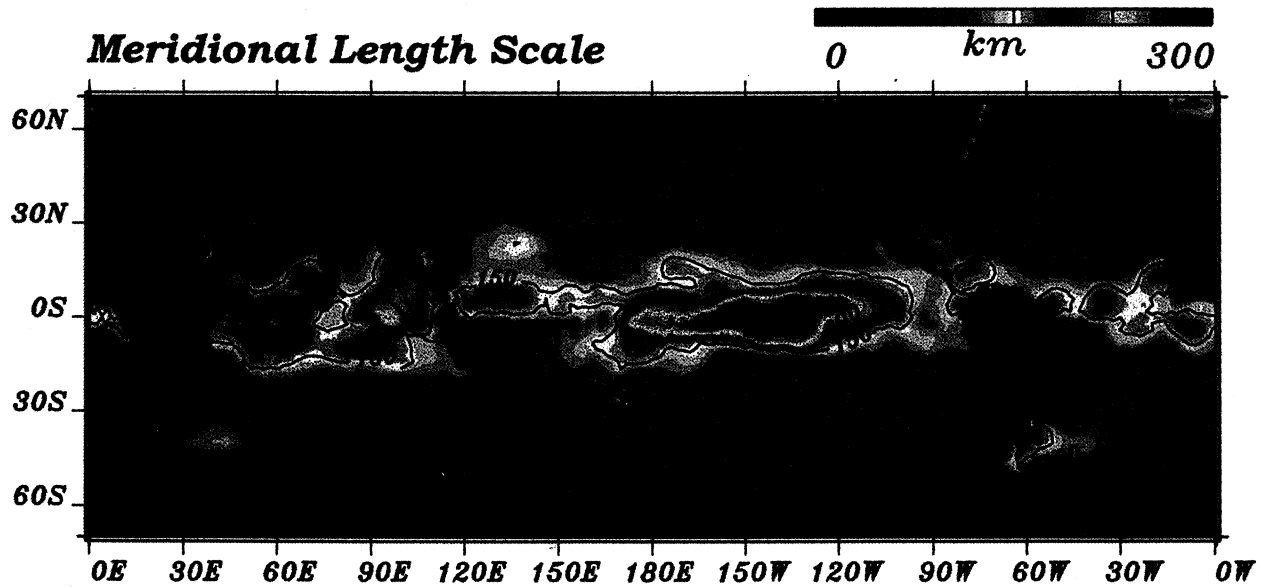


Plate 5. Meridional length scales are slightly smaller than the zonal scales and are larger than the Rossby radius of deformation at middle to high latitudes. Areas of large zonal and meridional scales are well correlated.

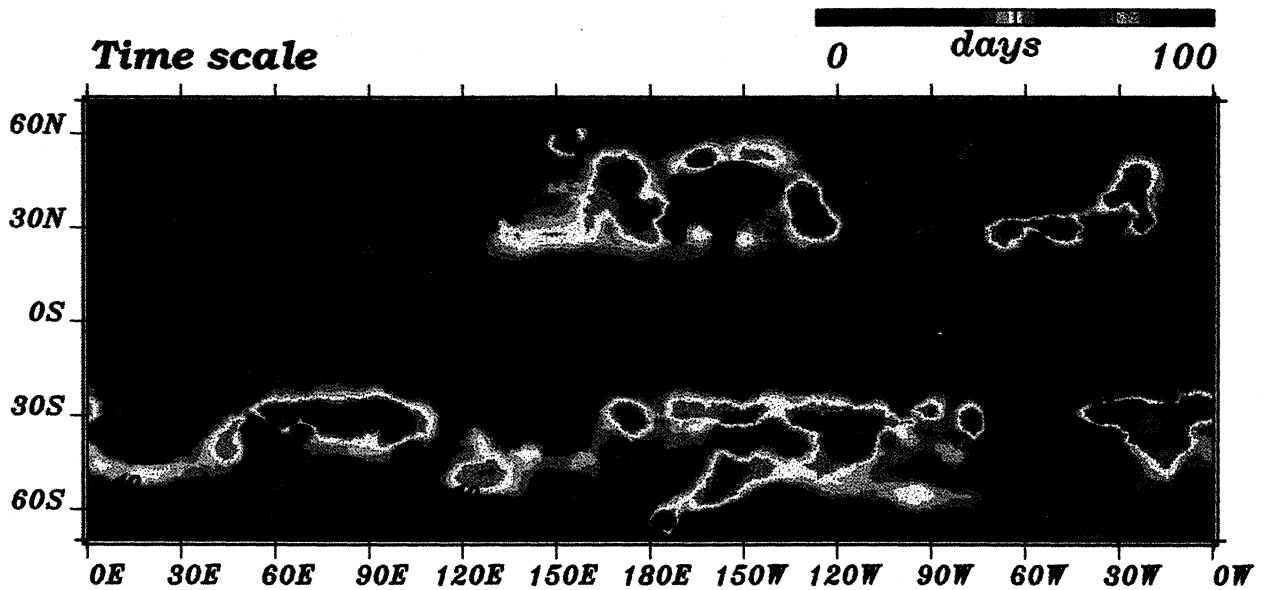


Plate 6. Timescale derived here is the time over which the peak amplitude of the binned covariance function decreases by $1/e$. This is not the time over which the covariance decreases by $1/e$ at the 0 meridional and zonal lag. Rather, this represents the decay time of propagating features.

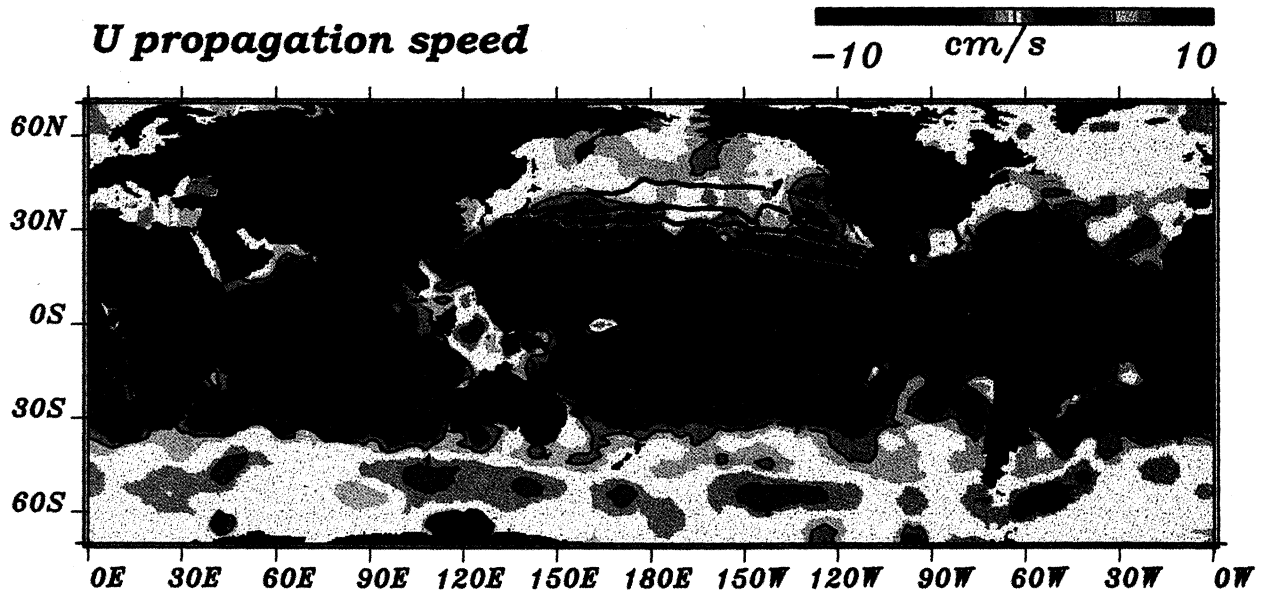


Plate 7. Zonal propagation speed (negative westward) increases toward the equator. The Antarctic Circumpolar Current appears to significantly affect the propagation speed of the mesoscale field. Black contour lines are based on the results derived here, and red contour lines are based on the expected linear quasi-geostrophic propagation speed using the Rossby radius of deformation from *Emery et al.* [1984]. The observed propagation speeds are in general agreement with those derived from theory at middle to high latitudes.

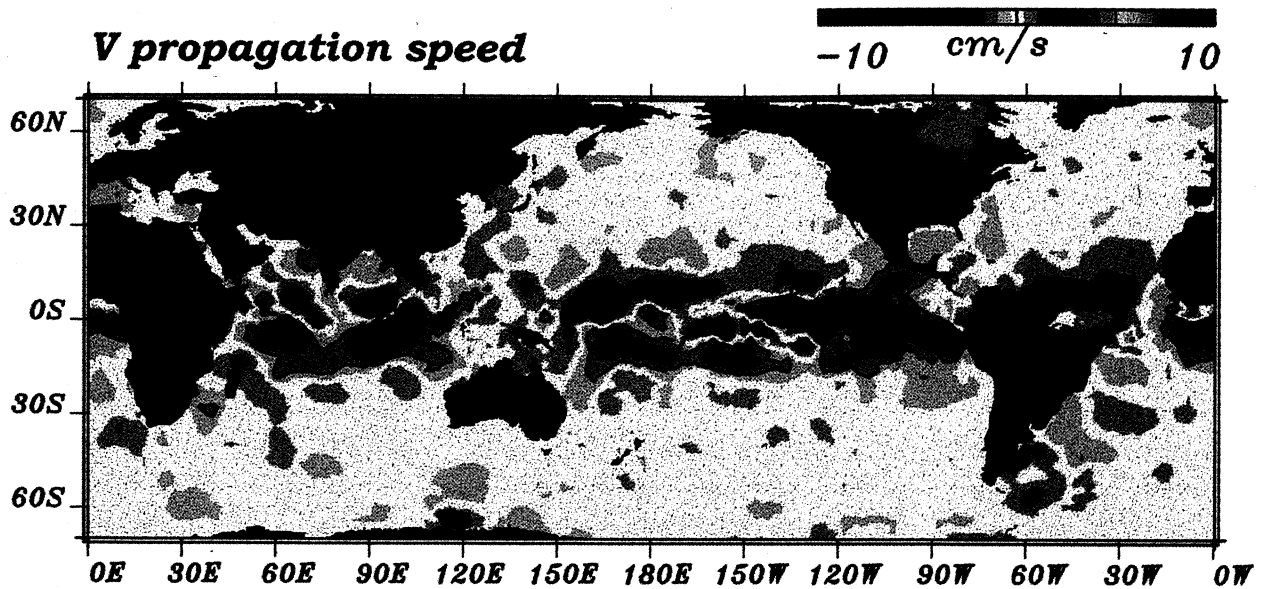


Plate 8. Meridional propagation speed indicates a divergence of eddies from the equator except in the eastern Pacific. At about 15° latitude, there is a convergence of the mesoscale field.

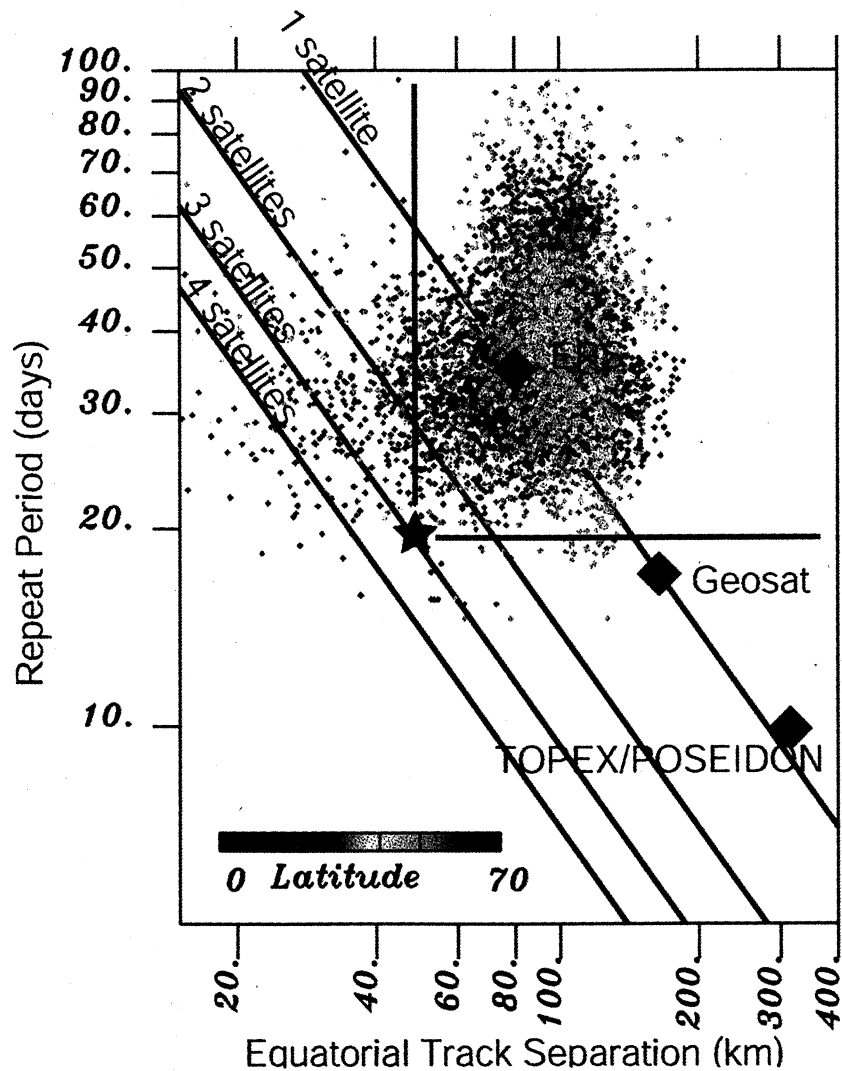


Plate 9. Mesoscale field zonal and temporal distributions provide an indication of the sampling required to synoptically observe the mesoscale variability. The sampling capabilities of a single satellite will generally fall on the one-satellite line (with some deviation due to orbit height). To provide the synoptic view of a majority of the mesoscale field, three coordinated satellites are required. However, these requirements may be relaxed if the data are used in conjunction with either statistical or numerical ocean models.

number of samples in each bin is generally above 2000 (Plate 1, bottom). Because we have presented the binned covariance function at lags of 10 days, the T/P ground tracks are dominant. At zero time lag, the ERS ground tracks are also apparent. At the 20-day time lag, interactions between the ERS and T/P ground tracks are strong.

4. Functional Fitting

In order to represent the mesoscale characteristic variations throughout the globe, we assume a functional form for the binned covariance. The functional form is fit to the binned covariance function at each point on the 2° grid. The spatial variations of the parameters describing the function are then presented. The function used to describe the mesoscale covariance is a Gaussian with separate meridional and zonal e -folding length scales, meridional and zonal propagation speeds, and a time e -folding scale:

$$R(x, y, t) = a^2 \exp \left\{ - \left[\frac{(x-ut)^2}{L_x^2} + \frac{(y-vt)^2}{L_y^2} + \frac{t^2}{T^2} \right] \right\}. \quad (2)$$

The values for x , y , and t are not taken as the bin position. As described in section 3, the data centroid within each bin gives its position. This functional form represents eddies as ellipses that propagate at fixed speeds in the meridional and zonal directions and decay with a given timescale. Certainly, more complicated functional forms may be applied. These may allow the ellipse major axis to be rotated from the purely meridional or the zonal directions. In addition, an alternate functional form may better represent the shape of the covariance function. However, the algorithm must apply this form throughout the globe, and it is difficult to provide a different form that simultaneously maintains similar simplicity and more accurately represents the mesoscale field throughout the world.

The functional fitting is performed by a least squares minimization. The minimization problem is nonlinear, and it is necessary to provide an accurate initial estimate for the functional parameters. The initial estimate uses propagation speeds based on computing the covariance centroid position at each time lag. Using the propagation speeds, the rate at which the peak covariance decays is computed to provide a time e -folding scale. Initial estimates of spatial length scales are based on an averaging length scale at each lagged time. The initial estimate of the covariance amplitude is taken as the observed zero lag amplitude. We solve the nonlinear least squares process by minimizing each parameter independently. The minimization with respect to each parameter is repeated iteratively until the squared error to the binned covariance is minimized.

5. Results

The parameters defining the functional form (2) are based on the binned covariance, which is computed on a regular 2° grid throughout the globe. Thus each parameter is examined on a 2° grid. The global grid of each parameter is smoothed to reduce noise. The smoothing is a simple boxcar function with meridional and zonal extents of 2° (a filter width of three grid points). The resulting parameters are presented in Plates 2 through 7.

The covariance amplitude (Plate 2) derived from the covariance function (the parameter a in (2)) is largest in the western boundary currents (Gulf Stream, Kuroshio, Aghulas Retroreflection, East Australian Current, and Brazil Current) with local peaks in the Gulf of Mexico and Madagascar current regions. Moderate amplitudes extend throughout the Antarctic Circumpolar Current and the eastern portions of the subtropical gyres. This would be expected in these regions, as the variability due to eddy activity is large [Zlotnicki *et al.*, 1989], and the mesoscale field derives its energy from baroclinic shear, which is highest in the western boundary current regions.

The covariance amplitude peaks here are less than the peak RMS variability observed by previous studies for several reasons. The large-scale variability (which had been removed before computing the binned covariance functions) adds significantly to the variability generated by the mesoscale field. The 2° grid on which the covariance is computed does not provide sufficient resolution to capture the localized peaks in the western boundary currents and their extensions. The Gaussian fit to the observed binned covariance function may not correctly represent the peak at the zero lag (the total variability).

The extent to which the assumed covariance function form (2) represents the observed covariance function is determined by examining the fraction of the observed covariance function explained by the fit form (Plate 3). The fraction of the observed covariance function explained is higher in the subtropics and midlatitudes than at the equator. Also, the fraction explained is very low near land, where eddies might be influenced strongly by shelf topography. Typical values of the fraction of the binned covariance explained are around 0.4 to 0.5. Many effects lead to lower values. For example, the assumed form is not capable of representing negative covariance values, or the binned covariance shape may not be close to Gaussian.

The zonal length scales are characterized by amplitudes over 300 km in the equatorial areas and amplitudes of 60 km in the subarctic (Plate 4). The idealized tests with the large-scale filtering indicate that in order for regions to be dominated by length scales greater than 200 km, there must be very little energy at shorter length scales. Thus, equatorial length scales are dominated by 300-km features.

According to linear quasi-geostrophic theory, anomalies on a beta plane propagate westward with a speed determined by the vertical stratification [Pedlosky, 1987]. The vertical stratification leads to an expected length scale, the Rossby radius deformation, which may be determined in combination with density observations. The Rossby radius of deformation determined by Emery *et al.* [1984] is contoured in red lines over the North Pacific Ocean (Plate 4). The general trends of the results here are in agreement with observations. Length scales decrease toward the poles, and the length scales in the western basins are larger than those in the east owing to the deepening pycnocline and thus changed vertical structure as illustrated by Chelton *et al.* [1998]. However, the length scales estimated here are generally larger than the Rossby radius of deformation. The ratio of observed zonal length scale to Rossby radius is about 2 for a Rossby radius of 150 km and about 4 for a Rossby radius of 20 km. Meridional length scales (Plate 5) have spatial variations similar to the zonal length scales, but meridional scales are slightly less than

the zonal scales. The implication is that mesoscale anomalies have a slightly greater zonal length than meridional length.

Comparing the length scales derived here to observed length scales, *Halliwel et al.* [1991] observed warm core eddy diameters of about 100 km and spatial decorrelation scales in the range from 70 to 80 km in the Georges Bank vicinity. Scales derived in the same area are slightly larger (100 to 110 km). *Hua et al.* [1986] use length scales of 180 km in the POLYMODE-LDE site (31°N) and 120 km in the MODE site (28°N) compared with about 100 km obtained here. *Le Groupe Tourbillon* [1983] observe length scales of about 70 km, compared with the 80 to 90-km scales in the same area derived here.

Previous works using altimeter data derive length scales using several methods. The first method uses covariance functions of only the data along each repeat pass. This method provides a one-dimensional covariance function (a function of lag distance along the ground track). The length scale may be defined by the first zero crossing of the covariance function, which is the L0 scale. For a Gaussian covariance function, as we fit to the binned covariance, there is no zero crossing. Thus a direct comparison of L0 scales to our length scales is difficult. *Le Traon et al.* [1990] compute along-track wave number spectra and autocorrelation of the Geosat ERM data. The L0 scales are 150-200 km for data 20°N to 30°N, 130-150 km for data 30°N to 40°N, and 110-120 km for data 40°N to 50°N. These values are slightly larger than the values obtained in this analysis.

Other length scales may be defined based on the one-dimensional along-track covariance function. *Stammer and Boning* [1992] compute L0, L1, and L2 length scales of Geosat ERM along track autocorrelation in 10° squares across the Atlantic Ocean. The L1 and L2 scales are defined by

$$\begin{aligned} L_1 &= \frac{1}{c(0)} \int_0^{L_0} c(s) ds \\ L_2 &= \frac{1}{c^2(0)} \int_0^{L_{\max}} c^2(s) ds, \end{aligned} \quad (3)$$

where $c(s)$ is the observed covariance and L_{\max} is the maximum lag. If we take L0 to be L_{\max} , then for a Gaussian function with a 100-km e -folding distance, the L1 scale is 91 km and the L2 length is 65 km (assuming L_{\max} is much larger than the 100-km e -folding scale).

The length scales derived here compare well with the *Stammer and Boning* [1992] L0 scales near the equator, though the scales derived here are smaller than their L0 scales near the poles. The *Stammer and Boning* [1992] L1 and L2 length scales are significantly less than the L0 scale, though they have similar spatial variations. The length scales of *Stammer and Boning* [1992] are generally higher in the central to eastern side of the basin, contrary to the results here. The later analysis of *Stammer* [1997] that optimally filters the T/P data provides L1 scales of 45 to 65 km at 60° latitude similar to the length scales in this analysis at the same latitude, though the L1 scales of *Stammer* [1997] near the equator reach only 120 km as opposed to 200 to 300 km in the analysis here.

Timescales may be defined in several ways. A timescale may be defined as the decorrelation time when viewing a single point in space. This is the timescale computed by *Stammer* [1997] using 3 years of T/P data, and timescales of 25 to 30 days are typically observed throughout the world (the

scale used by *Stammer* [1997] in time is an L1 scale). Also of interest to the mesoscale field is the decay time of individual eddies as they propagate. The decay time of individual eddies is represented in the functional form here. The typical e -folding time of the mesoscale field is between 20 and 60 days (Plate 6). Longer time periods are common throughout midlatitudes. Shorter timescales occur in equatorial regions dominated by fast Kelvin waves. The timescales derived by *Stammer* [1997] are the decorrelation times in an Eulerian coordinate system, that is, when viewing a single point in space. Because the timescales here are based on decorrelation when viewing a feature in a linearly moving reference, the timescales are longer.

Schouten et al. [2000] examine the rings shed from the Agulhas current into the Atlantic Ocean around the southern tip of Africa. The upper bound of ring lifetimes is 3.5 years, and the typical e -folding scale is about 150 days. Many of the observed ring events follow paths that change direction with time. One reason that the results here indicate shorter timescales is because this analysis views the properties of features in a coordinate system that moves linearly in time and uses the same linear propagation speed for each feature. *Schouten et al.* [2000] view the properties of each feature in individual coordinate frames that have velocities varying in time to move with each individual feature.

The zonal propagation field (Plate 7) contains the expected westward drift with a decrease in westward speed away from the equator. The Antarctic Circumpolar Current region contains eastward (positive) propagation possibly due to the advection by the Antarctic Circumpolar Current. *Hughes et al.* [1998] examine the propagation direction and wavelengths using 4.8 months of SST and SSH from the ERS-1 satellite as well as the FRAM model. Eastward propagation is observed in the SST and SSH throughout the same region in which eastward propagation is observed here.

According to linear quasi-geostrophic theory, anomalies on a beta plane propagate westward with a speed determined by the Rossby radius deformation. Of course, mesoscale eddy genesis from baroclinic shear is a nonlinear instability process, and the magnitude of nonlinear momentum terms within the eddy field is as large as other linear terms. Thus the mesoscale field is certainly nonlinear. It is interesting to compare the propagation speeds to linear theory to examine the effect of the nonlinearities. To compare with theoretical values, we compute the Rossby wave phase speed based on

$$c = \frac{\beta}{k^2 + l^2 + 1/R^2}, \quad (4)$$

where β is the meridional gradient of the Coriolis parameter, k is the zonal wave number, l is the meridional wave number, and R is the Rossby radius of deformation.

The wave numbers are based on the zonal length scales derived here:

$$k = \frac{2\pi}{3L_x} \quad l = \frac{2\pi}{3L_y} \quad (5)$$

Thus the wavelength is taken to be 3 times the e -folding length scale.

The theoretical Rossby wave speed is contoured in red lines on the plot of the derived zonal propagation speed (Plate 7). Propagation speeds are higher in the western basins than in the eastern basins owing to the deeper thermocline in the west. The propagation speeds are roughly in agreement with

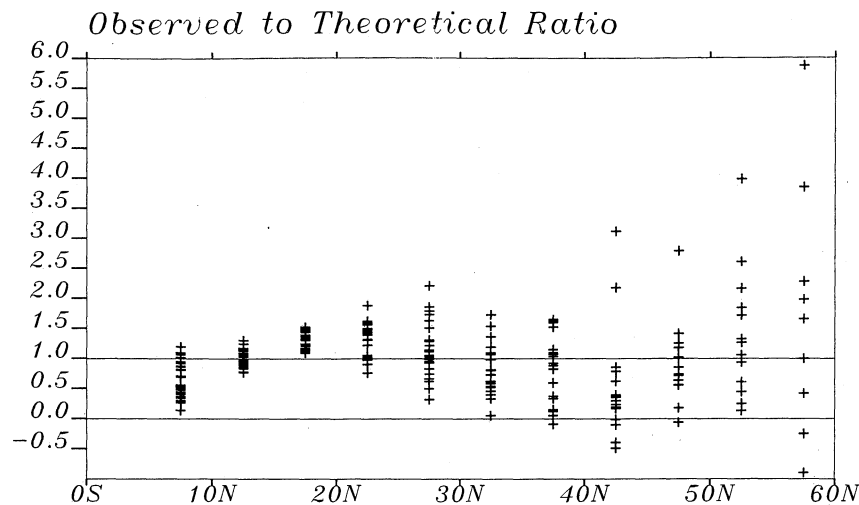


Figure 3. Ratio of observed propagation speed to the linear Rossby wave propagation speed indicates a reasonable comparison at midlatitudes.

the theoretical values. However, the results are very sensitive to the relation between the length scale and the wave numbers defined in (4). Small changes in the relation can produce different results. The ratio of observed to theoretical propagation speed in the North Pacific (Figure 3) is different from the results of *Chelton and Schlax* [1996], who find propagation speeds of about 5 cm/s at 30°N. Their observed propagation speed at 30°N is about twice that predicted by theory. The results here are more consistent with the theoretical propagation speeds of 2 to 3 cm/s. Thus the mesoscale features propagate at speeds closer to the theoretical than do the features examined by *Chelton and Schlax* [1996]. One possible explanation is the contribution of the atmosphere-ocean coupling acting at large scales as suggested by *White* [2000]. However, numerical model experiments indicate large-scale features propagating at twice the theoretical speed even without wind forcing [*Jacobs et al.*, 1994]. *Killworth et al.* [1997] explain the higher than theoretical observed propagation speeds by background potential vorticity interactions. This remains an active area of investigation.

The meridional propagation field (Plate 8) generally indicates a divergence from the equator. Northward eddy propagation appears on the northern side of the equator and southward eddy propagation on the southern side of the equator. This divergence surrounding the equator is accompanied by a convergence of the eddy field away from the equator. The northward propagation on the northern side of the equator ends at about 15°N. Similarly, the southward propagation south of the equator ends at about 15°S. Thus eddies tend to drift away from the equator and toward 15° latitude.

6. Sampling Requirements

We compare the sampling capabilities of the Geosat, T/P, and ERS 35-day repeat orbits relative to the mesoscale characteristics derived in this analysis (Plate 9). We use the term "design point" to refer to the combination of the distance between ground tracks at the equator and repeat period of a

particular orbit configuration. For a single altimeter satellite, the product of the repeat cycle period and the distance between ground tracks at the equator is proportional to the orbit period. Thus there is a trade-off between the spatial sampling capability and temporal resolution. Each satellite can resolve only features that have length scales greater than the ground track separation and timescales greater than the repeat cycle time. The temporal and spatial resolution of an altimeter satellite may be viewed as an area covered in the wavelength-time period domain. Only wavelengths and time periods to the upper right of the satellite design point in wavelength-time period space are resolvable by a single satellite altimeter. This area may be restricted further by additional considerations such as the Nyquist frequency and the exact pattern in which the tracks are sampled. The design points of previous altimeter satellites are shown in Plate 9. If the orbit period of all satellites were equal, then all satellite design points would fall on the same line. However, since the T/P orbit period is longer than both the Geosat ERM and ERS orbit periods (since T/P is at higher altitude), the T/P design point falls slightly above the Geosat ERM and ERS line.

At the mission design stage, the design point of a single satellite altimeter may be placed anywhere along the single satellite line. The choice of time and length scales measured may be made to cover the largest portion of the mesoscale field as possible. The mesoscale characteristic time and zonal length scales are shown by the dots in Plate 9. The zonal length scale is divided by the cosine of latitude to account for the convergence of the satellite ground tracks with latitude. The design point for the single altimeter should be chosen so that the area to the upper right of the point encompasses the largest possible portion of the mesoscale field. None of the single altimeter systems is capable of covering a majority of the range of the mesoscale field characteristics.

Two altimeter satellites may be coordinated in many different ways. For example, two satellites may be placed in the same ground track separated to reduce the repeat cycle by half. The satellites may also be placed so that the ground tracks interleave, reducing the spatial separation of the ground tracks by half. By coordinating two satellites in this manner

the design point of the two-satellite system falls on a line that is to the left of the line of design points for a single-satellite system. The design point of a two-satellite system covers a larger region of the wavelength/time period domain than the single-satellite design point. Three coordinated satellites with equatorial track separation of 50 km and a 20-day repeat period are needed to cover a large portion of the mesoscale circulation. A less efficient system may be composed of two satellites with a 60-km equatorial separation and 25-day repeat. While one satellite is not capable of synoptically observing a majority of the mesoscale field, there are choices that provide better sampling capability. Of the previous ground tracks, the ERS 35-day repeat encompasses the largest portion of the mesoscale characteristics.

It should be noted that significant relaxation of these requirements might be made by using the altimeter data in either statistical or numerical ocean models. The above requirements are based on the assumption that we have no prior estimate of the ocean mesoscale state and we have no knowledge of its dynamics. Thus the analysis must construct the state based solely on the observations over one satellite repeat cycle. Typical lifetimes of eddies are from months to years [Schouten et al., 2000]. Thus data that may be a month old still have information within it that is useful for estimating the present ocean mesoscale state. Techniques that properly join together information over a month or longer can reduce the requirements. The mesoscale characteristics derived here can provide significantly improved optimal interpolation of present altimeter data by allowing an observed feature to subsequently propagate away from a satellite ground track. Assimilating the observed mesoscale field into a numerical model allows the model to evolve and propagate observed eddy features. The altimeter data provide small corrections to the model state to maintain the mesoscale field accuracy [Smedstad et al., 1997].

7. Conclusions

The length scales observed from the altimeter data are in general agreement with previous results. The spatial variations in the length scales are in agreement with Rossby radii, but the length scales are larger than the Rossby radii. Propagation speeds are in agreement with linear quasi-geostrophic theory. Meridional eddy propagation velocities indicate a divergence of eddies at the equator and a convergence of the eddy field at about 15° in both the Southern and Northern Hemispheres. In order to continuously observe mesoscale features, a system of at least three coordinated altimeter satellites would be needed. However, this requirement may be relaxed by using the data through more advanced techniques such as assimilating the observations into ocean models.

Acknowledgments. We are grateful to the two anonymous reviewers who dedicated their time and effort to very significantly improve this manuscript. This work was sponsored by the Space and Naval Warfare Systems Command (program element 0603207N) as part of the Altimeter Data Fusion Center Support Project and the Office of Naval Research (program element 601153N) as part of the project Dynamical Linkage of the Asian Marginal Seas. This paper is NRL contribution JA/7323-99-0030.

REFERENCES

- Aoki, S., and S. Imawaki, Eddy activities of the surface layer in the western North Pacific detected by satellite altimeter and radiometer, *J. Oceanogr.*, **52**, 457-474, 1996.
- Auer, S. J., Five-year climatological survey of the Gulf Stream system and its associated rings, *J. Geophys. Res.*, **92**, 11,709-11,726, 1987.
- Chelton, D. B., and M. G. Schlax, Global observations of oceanic Rossby waves, *Science*, **272**, 234-238, 1996.
- Chelton, D. B., R. A. DeSzoeke, and M. G. Schlax, Geographical variability of the first baroclinic Rossby radius of deformation, *J. Phys. Oceanogr.*, **28**, 433-460, 1998.
- Cheney, R. E., J. G. March, and G. D. Beckley, Global mesoscale variability from collinear tracks of Seasat altimeter data, *J. Geophys. Res.*, **88**, 4343-4354, 1983.
- Emery, W. J., W. G. Lee, and L. Magaard, Geographic and seasonal distribution of Brunt-Väisälä frequency and Rossby radii in the North Pacific and North Atlantic, *J. Mar. Res.*, **34**, 365-385, 1984.
- Fu, L. L., On the wavenumber spectrum of oceanic mesoscale variability observed by the Seasat altimeter, *J. Geophys. Res.*, **88**, 4331-4341, 1983.
- Fu, L. L., and V. Zlotnicki, Observing oceanic mesoscale eddies from GEOSAT altimetry: Preliminary results, *Geophys. Res. Lett.*, **16**, 457-460, 1989.
- Fu, L. L., E. J. Christensen, C. A. Yamarone, M. Lefebvre, Y. Menard, M. Dorrer, and P. Escudier, TOPEX/Poseidon mission overview, *J. Geophys. Res.*, **99**, 24,369-24,382, 1994.
- Gilson, J., D. Roemmich, B. Cornuelle, and L. L. Fu, Relationship of TOPEX/Poseidon altimetric height to steric height and circulation in the North Pacific, *J. Geophys. Res.*, **103**, 27,947-27,965, 1998.
- Halliwel, G. R., Jr., and C. N. K. Mooers, The space-time structure and variability of the shelf water-slope water and Gulf Stream surface temperature fronts and associated warm-core eddies, *J. Geophys. Res.*, **84**, 7707-7725, 1979.
- Halliwel, G. R., Jr., Y. J. Ro, and P. Cornillon, Westward-propagating SST anomalies and baroclinic eddies in the Sargasso Sea, *J. Phys. Oceanogr.*, **21**, 1664-1680, 1991.
- Hallock, Z. R., J. L. Mitchell, and J. D. Thompson, Sea surface topographic variability near the New England Seamounts: An intercomparison among in situ observations, numerical simulations, and Geosat altimetry from the Regional Energetics Experiment, *J. Geophys. Res.*, **94**, 8021-8028, 1989.
- Hua, B. L., J. C. McWilliams, and W. B. Owens, An objective analysis of the POLYMODE Local Dynamics Experiment, part II, Streamfunction and potential vorticity fields during the intensive period, *J. Phys. Oceanogr.*, **16**, 506-522, 1986.
- Hughes, C. W., M. S. Jones, and S. Carnochan, Use of transient features to identify eastward currents in the Southern Ocean, *J. Geophys. Res.*, **103**, 2929-2943, 1998.
- Ichikawa, K., and S. Imawaki, Life history of a cyclonic ring detached from the Kuroshio Extension as seen by the Geosat altimeter, *J. Geophys. Res.*, **99**, 15,953-15,966, 1994.
- Jacobs, G. A., and J. L. Mitchell, Combining multiple altimeter missions, *J. Geophys. Res.*, **102**, 23,187-23,206, 1997.
- Jacobs, G. A., H. E. Hurlburt, J. C. Kindle, E. J. Metzger, J. L. Mitchell, W. J. Teague, and A. J. Wallcraft, Decade-scale trans-Pacific propagation and warming effects of an El Niño anomaly, *Nature*, **370**, 360-370, 1994.
- Killworth, P. D., D. B. Chelton, and R. A. de Szoeke, The speed of observed and theoretical long extratropical planetary waves, *J. Phys. Oceanogr.*, **27**, 1946-1966, 1997.
- Kuragano, T., and M. Kamachi, Global statistical space-time scales of oceanic variability estimated from the TOPEX/Poseidon altimeter data, *J. Geophys. Res.*, **105**, 955-974, 2000.
- Le Groupe Tourbillon, The *Tourbillon* experiment: A study of a mesoscale eddy in the eastern North Atlantic, *Deep Sea Res.*, **30**, 475-511, 1983.
- Le Provost, C., M. L. Genco, F. Lyard, P. Vincent, and P. Canceil, Spectroscopy of the world ocean tides form a finite element hydrodynamic model, *J. Geophys. Res.*, **99**, 24,777-24,798, 1994.
- Le Traon, P. Y., M. C. Rouquet, and C. Boissier, Spatial scales of mesoscale variability in the North Atlantic as deduced from Geosat data, *J. Geophys. Res.*, **95**, 20,267-20,285, 1990.

- McCarthy, M. C., L. D. Talley, and D. Roemmich, Seasonal to interannual variability from expendable bathythermograph and TOPEX/Poseidon altimeter data in the South Pacific subtropical gyre, *J. Geophys. Res.*, *105*, 19,535-19,550, 2000.
- McWilliams, J. C., W. B. Owens, and B. L. Hua, An objective analysis of the POLYMODE Local Dynamics Experiment, part I, General formalism and statistical model selection, *J. Phys. Oceanogr.*, *16*, 483-504, 1986.
- Mercier, H., and A. C. de Verdiere, Space and time scales of mesoscale motions in the eastern North Atlantic, *J. Phys. Oceanogr.*, *15*, 171-183, 1985.
- Pedlosky, J., *Geophysical Fluid Dynamics*, 2nd ed., Springer-Verlag, New York, 1987.
- Richman, J. G., C. Wunsch, and N. G. Hogg, Space and time scales of mesoscale motion in the western North Atlantic, *Rev. Geophys.*, *15*, 385-420, 1977.
- Schouten, M. W., W. P. M. de Ruijter, and P. J. van Leeuwen, Translation, decay, and splitting of Agulhas rings in the southeastern Atlantic Ocean, *J. Geophys. Res.*, *105*, 21,913-21,925, 2000.
- Smedstad, O. M., D. N. Fox, H. E. Hurlburt, G. A. Jacobs, E. J. Metzger, and J. L. Mitchell, Altimeter data assimilation into a 1/8 degree eddy resolving model of the Pacific Ocean, *J. Meteorol. Soc. Jpn.*, *75*, 429-444, 1997.
- Stammer, D., Global characteristics of ocean variability estimated from regional TOPEX/Poseidon altimeter measurements, *J. Phys. Oceanogr.*, *27*, 1743-1769, 1997.
- Stammer, D., and C. W. Boning, Mesoscale variability in the Atlantic Ocean from Geosat altimetry and WOCE high-resolution numerical modeling, *J. Phys. Oceanogr.*, *22*, 732-752, 1992.
- Tai, C. K., and W. B. White, Eddy variability in the Kuroshio Extension as revealed by Geosat altimetry: Energy propagation away from the jet, Reynolds stress, and seasonal cycle, *J. Phys. Oceanogr.*, *20*, 1761-1777, 1990.
- Teague, W. J., M. J. Carron, and P. J. Hogan, A comparison between the Generalized Digital Environmental Model and Levitus climatologies, *J. Geophys. Res.*, *95*, 7167-7183, 1990.
- Teague, W. J., Z. R. Hallock, G. A. Jacobs, and J. L. Mitchell, Kuroshio sea surface height fluctuations observed simultaneously with inverted echo sounders and TOPEX/Poseidon, *J. Geophys. Res.*, *100*, 24,987-24,994, 1995.
- White, W. B., Tropical coupled Rossby waves in the Pacific Ocean-atmosphere system, *J. Phys. Oceanogr.*, *30*, 1245-1264, 2000.
- Zlotnicki, V., L. L. Fu, and W. Patzert, Seasonal variability in global sea level observed with Geosat altimetry, *J. Geophys. Res.*, *94*, 17,959-17,969, 1989.
-
- C. N. Barron, G. A. Jacobs, and R. C. Rhodes, Naval Research Laboratory, Code 7323, Stennis Space Center, MS 39529, USA. (barron@nrlssc.navy.mil, jacobs@nrlssc.navy.mil, rhodes@nrlssc.navy.mil)

(Received October 5, 2000; revised May 3, 2001; accepted May 10, 2001.)